Importance of valence-band anharmonicity and carrier distribution for third- and fifth-harmonic generation in Si:B pumped with intense terahertz pulses

Fanqi Meng [1,*] Frederik Walla [1] Qamar ul-Islam,[1] Alexej Pashkin [2] Harald Schneider [2] Christoph Jungemann [3]
Mark D. Thomson[1,†] and Hartmut G. Roskos[1,‡]

[1]*Physikalisches Institut, Goethe-Universität Frankfurt, 60438 Frankfurt am Main, Germany*
[2]*Institute of Ion Beam Physics and Materials Research, Helmholtz-Zentrum Dresden-Rossendorf, 01328 Dresden, Germany*
[3]*Institut für Theoretische Elektrotechnik, RWTH Aachen, 52062 Aachen, Germany*

We observe third-harmonic generation (THG) and fifth-harmonic generation (FHG) of free holes in the valence band of bulk Si:B at cryogenic temperature upon irradiation with intense terahertz pulses from a free-electron laser, polarized along the Γ-X direction. The intensities of both signals increase as a function of pulse energy following power laws with respective exponents of 4.2 and 6.2, larger than the exponents of 3 and 5 expected for $\chi^{(3)}$ and $\chi^{(5)}$ processes with constant susceptibilities and a fixed number of holes. The larger values are attributed to the increase in the density of mobile holes, which results from impact ionization of boron dopants by thermally activated holes in the electric field of the terahertz pulses as already observed in our studies of THG in Si:B reported in Phys. Rev. B **102**, 075205 (2020). We apply Monte Carlo simulations of the nonlinear heavy- and light-hole field response, coupled with a finite-difference time-domain treatment of the pump-pulse propagation in the sample, which reproduce the experimental THG:FHG intensity ratio reasonably well. An analysis of the local response demonstrates that, in our pump regime, the harmonic generation is dominated by the band anharmonicity as opposed to the energy-dependent momentum scattering rates or interband scattering. Comparison with the results of a simple one-dimensional model and scrutiny of the three-dimensional band structure shows that one must account for the extent of the carrier distribution transverse to the Γ-X axis as the anharmonicity grows rapidly away from this axis.

I. INTRODUCTION

Frequency multiplication—or higher-harmonic generation—lies at the core of nonlinear optics [1,2]. Several photons combine to generate single photons of higher energy in materials with a field-strength-dependent electric susceptibility. Classical semiconductors have been explored as such nonlinear materials. In studies with radiation with a photon energy much smaller than the energy band gap, it was found that the nonlinearity of mobile charge carriers is much stronger than that of bound ones [3–5]. This led to intensive studies of doped semiconductors [6–10] not least with the goal in mind to develop frequency converters for high-power terahertz radiation [10,11]. In the case of electrons in the conduction band of such semiconductors, the origin of the nonlinearity is attributed to band nonparabolicity [4], the energy dependence of the momentum scattering time [5,12] or to both [8,9]. However, the mechanisms of frequency multiplication by holes in the valence band have not yet been analyzed in a corresponding manner [9].

Here, we investigate *p*-doped bulk Si. The centrosymmetric crystal structure only permits generation of odd harmonics of the center frequency of the incoming electromagnetic wave.

In the studies cited above, no higher harmonic than the third was observed because of the limited field strength. In our previous publication [1], we also studied third-harmonic generation (THG) by free holes in the valence band of Si:B with the sample at cryogenic temperature [1]. It was excited by intense free-electron laser (FEL) pulses at 1.56 THz. In this publication, we now report the observation of both THG and fifth-harmonic generation (FHG). The detection of a signal at the fifth harmonic became possible by reducing the photon energy of the terahertz pulses and by increasing the pulse intensity. The results of spatiotemporal Monte Carlo (MC) simulations can reproduce the observed THG:FHG ratio reasonably well, whereas an analysis of the local velocity vs wave-vector response supports that for these pump fields, the HG mechanism is dominated by the band structure anharmonicity, which depends critically on the extent of the carrier distribution perpendicular to the driving field polarization.

II. EXPERIMENTAL RESULTS

The experiments were carried out at the FELBE facility of the Helmholtz-Zentrum Dresden-Rossendorf. FELBE delivers transform-limited multicycle terahertz pulses which are tunable from 1.2 up to 75 THz at a pulse repetition rate of 13 MHz. We chose a radiation frequency of 1.29 THz, close to the facility's lower limit. The ponderomotive energy of the holes in the Si specimen is higher at low frequency [13] with the consequence that the charge carriers are driven further out

*f.meng@physik.uni-frankfurt.de
†thomson@physik.uni-frankfurt.de
‡roskos@physik.uni-frankfurt.de

into **k** space by the (linearly polarized) electric field of the terahertz pulses. The nonlinear susceptibility is then higher [9,10].

The experimental setup was similar to that of our experiments reported in Ref. [1]. The sample under test was again a commercial ⟨100⟩-oriented Si:B specimen (purchased from MTI Corp.) with a boron density of 5×10^{16} cm^{-3} and a wafer thickness of 275 μm. All measurements were carried out at a temperature of 10 K. The FEL radiation was polarized along one of the equivalent ⟨100⟩ axes, accelerating holes along the Γ-X direction in momentum space. A multilayer metal-mesh low-pass filter (LP70 cm^{-1} from QMC Instruments Ltd.) with a steep frequency cutoff at 2.1 THz was placed in front of the sample in order to reduce the amount of third harmonic (TH) radiation generated in the FEL itself. Two high-pass filters (multilayer metal-mesh filters HP74 and HP100 cm^{-1} from QMC Instruments Ltd.) placed behind the sample strongly reduced the transmitted fundamental pump intensity (with a residual transmittance of 1.1×10^{-7}) in order to improve the dynamic range of the measured higher-harmonic signals. The transmitted radiation was detected with a liquid-helium-cooled bolometer after having passed through a Fourier-transform infrared spectroscopy setup for spectral analysis.

Figure 1(a) presents spectra of the radiation detected at various pump intensities (black, blue and red curves). The green curve is a reference spectrum obtained at the highest pump intensity with an undoped Si sample [high-resistivity (HR) Si with a specific resistance > 12 kΩ cm at room temperature, purchased from University Wafer, Inc.). In that spectrum, transmission peaks at 1.29 and 4.07 THz represent the pump frequency and the leaked FEL-intrinsic third harmonic radiation. Interestingly, the latter (also observed in Ref. [1]) is slightly blueshifted against the value 3×1.29 THz for unknown reasons. The spectra of the doped Si sample also show these two features but exhibit in addition the third and fifth harmonic (FH) of the pump frequency, at 3.87 and 6.45 THz, respectively (the latter only at high pump intensity). As these signals only appear in the doped sample, they are identified as waves newly generated by either the dopant atoms or the free charge carriers. The dependence of the signal strengths of these two lines on the pump intensity allow to assign the origin of the waves to free holes, see below and in Ref. [1].

Since the spectra of the newly generated TH and the leaked 4.07-THz wave partially overlap, we used two Gaussian-shaped spectral lines to fit the measured spectra and to extract the intensity of the newly generated TH. The fitting result for a pump pulse energy of 78.1 nJ is shown in the inset of Fig. 1(a).

Figure 1(b) displays the measured pulse intensities of the transmitted wave at the fundamental frequency (denoted by the letter I, black stars) as well as those of the newly generated TH signal ($I_{3\omega}$, blue squares) and FH signal ($I_{5\omega}$, red circles) as a function of the pump pulse energy, from 31.2 to 106.7 nJ measured in front of the sample, which corresponds to a peak intensity I_ω of the incoming pulses ranging from 0.95 to 3.25 MW/cm^2, based on the estimated diameter of the focal spot (400 μm) and pulse duration (23-ps full width at half maximum). These intensity values are corrected for the measured transmission of the high-pass filters at each harmonic. As expected, the intensity of the transmitted fundamental is
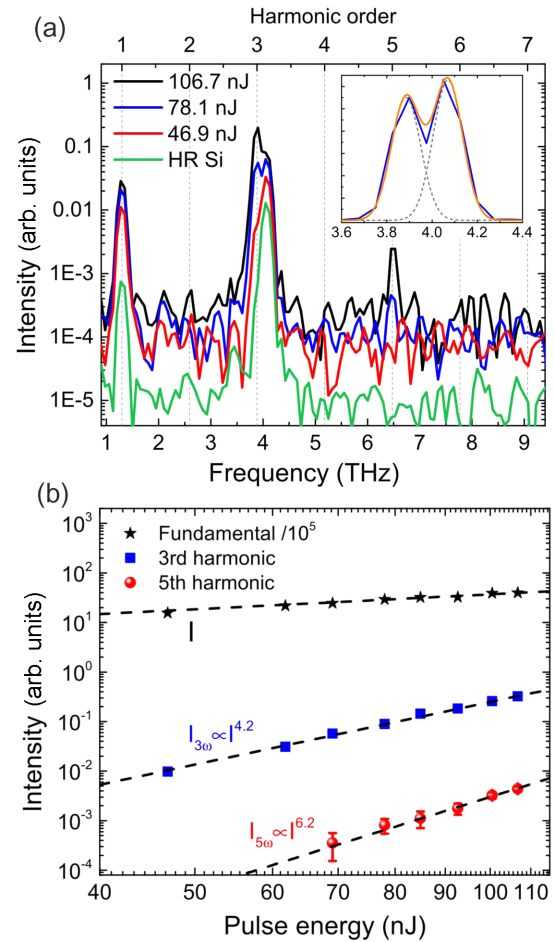

FIG. 1. Experimental results. (a) Transmittance/emittance spectra of the Si:B sample exposed to 1.29-THz radiation at the three pump pulse energies of 46.9, 78.1, and 106.7 nJ (red, blue, and black curves, power measured directly in front of the sample). Also included is the transmittance spectrum of the undoped HR Si sample for a pump pulse energy of 106.7 nJ (green curve, scaled down by a factor of 100 for better visibility in the logarithmic plot). The inset shows the 78.1-nJ signal around 4.0 THz also on a linear intensity scale (blue line). The spectrum consists of the FEL-immanent 4.07-THz line and the Si-generated THG signal at 3.87 THz. The orange curve displays the fit function composed of two Gaussians (which are shown individually as gray dashed curves). Their line widths are each set to 65 GHz.(b) Black stars: Measured transmitted intensity of the fundamental as a function of the pulse energy of the FEL beam. The black dashed line represents the linear dependence of the intensity as a function of the pump pulse energy. The blue squares represent the measured THG intensity, the blue dashed line a power law with an exponent of 4.2. The red spheres represent the measured FHG intensity with error bars based on the rms noise level. The red dashed line corresponds to a power-law dependence with an exponent of 6.2.

directly proportional to the pump pulse energy [black dashed line in Fig. 1(b)]. The intensities of the TH and FH pulses exhibit power-law dependencies $I_{m\omega} \propto I_\omega^{m+\eta}$ with $m = 3$ and 5, respectively, and $\eta = 1.2$ for both cases. These dependencies are plotted as blue and red dashed lines in Fig. 1(b). Expressed in terms of susceptibilities, the dependencies are $I_{m\omega} \propto (\chi^{(m)})^2 I_\omega^m$ with pump-intensity-dependent $\chi^{(m)}$ values. Since
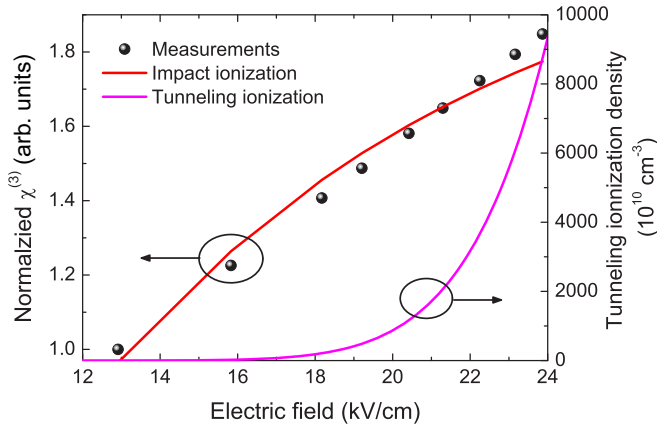
FIG. 2. Circles: $\chi^{(3)}$ as a function of the electric radiation field of the pump pulses inside the Si sample. The $\chi^{(3)}$ values are normalized to the value at the lowest field of 12.9 kV/cm. Red curve: Simulated $\chi^{(3)} = \chi_0^{(3)} n_d$, where $\chi_0^{(3)}$ is the third-order susceptibility of a single free hole, and n_d represents the free hole density, i.e., the sum of the residual free holes at 10 K and the free holes generated via impact ionization. Magenta curve: Estimated density of holes created by tunneling ionization.

the FHG intensities are relatively weak, we include the root-mean-square noise level of each measurement as error bars.

If the THG and FHG processes were due to the nonionized impurity atoms, one would expect $\eta = 0$ (or possibly $\eta < 0$ with ionization occurring). The fact that $\eta > 0$, leads to the conclusion that THG and FHG arise from free holes whose density increases with rising intensity due to impurity ionization (see below), starting from the density of thermally activated free holes [14] in the valence band of Si:B at a temperature of 10 K. That the fitted value of η is the same for both THG and FHG is also reasonable as both $\chi^{(3)}$ and $\chi^{(5)}$ should be proportional to the effective average hole density during the pump pulse [4].

III. IONIZATION OF DOPANTS

Following our procedure in Ref. [1] (i.e., scaling out a cubic dependence for the single-hole TH emission) we derived $\chi^{(3)}$ values from the measured data as a function of the electric radiation field within the Si specimen. The results are shown as black circles in Fig. 2. In our previous work, the electric field of the terahertz pulses was limited to 12 kV/cm, the ionization process was attributed to impact ionization, whereas direct tunneling ionization was expected to dominate above our highest field values. In the present paper, the maximum electric field reached is 24 kV/cm. Since the fundamental frequency (1.29 THz) is similar with the frequency (1.56 THz) used in the previous experiments, we took the impact ionization model of Eq. (3) in Ref. [1] with the same parameter $E_0 = 11.3$ kV/cm, to fit the field dependence of $\chi^{(3)}$ of Fig. 2. We integrate the ionization rate based on the time-dependent field of the pump pulse to yield a measure of the effective relative hole density for each peak field value. The fit curve (red line in Fig. 2) reproduces the experimental data well and, hence, accounts for the power-law exponents in Fig. 1. Whereas the impact ionization model has an exponential field

dependence for $E \ll E_0$, in our field range the ionization rate is already in saturation, resulting in the slower observed polynomial dependence.

We also calculated the hole density expected by tunneling ionization using Eq. (B1) in Ref. [1]. The result is shown by the magenta-colored curve in Fig. 2. The electric-field dependence is far more nonlinear than that of the experimentally determined $\chi^{(3)}$, which rules out direct tunneling as the main contribution to the ionization process at the relevant electric fields. This demonstrates that impact ionization is still the most important ionization mechanism at electric fields as high as 24 kV/cm. As one also notes that the measured $\chi^{(3)}$ starts to exceed the prediction of impact ionization at around 24 kV/cm, which indicates that the contribution of direct tunneling ionization starts to become important.

We note in passing that Eq. (B1) of Ref. [1] leads to unrealistically large density values to be expected for tunneling ionization. For an electric field of 24 kV/cm, (B1) yields a density of 1×10^{14} cm^{-3}, whereas impact ionization generates a density on the order of 1×10^{11} cm^{-3}. The tunneling-ionization model is known to overestimate the tunneling rate. Dargys and Žurauskas studied tunneling ionization of acceptors in GaAs [15] and found that the simulations with this model predicted an ionization rate which was more than one order of magnitude higher than measured in the experiments. The model needs refinement in the future. We expect, however, the exponential rise to survive.

IV. MONTE CARLO TIME-DOMAIN SIMULATIONS

We now address theoretically the origin of the $\chi^{(3)}$ and $\chi^{(5)}$ nonlinearities for the band carriers. As stated in the introduction, the literature discusses the respective roles of: (i) the band anharmonicity and (ii) the energy dependence of the carrier momentum relaxation rate as the main mechanisms which lead to frequency multiplication (although rigorously, the scattering rates indeed depend on the precise band structure). In order to analyze the effective contribution of each mechanism in our case, we performed a series of simulations with an established Monte Carlo method [16,17] which treats the time-dependent velocity response of an ensemble of holes, including all valence bands—i.e., light-hole (lh), heavy-hole (hh) and split-off bands (the latter having negligible occupation here), a realistic band structure based on a nonlocal empirical pseudopotential method [18], and acoustic-/optical-phonon scattering including interband processes as well as ionized impurity scattering [19]. As presented below, we also applied a simplified one-dimensional (1D) model where one only considers the equation of motion for a scalar value $\langle k_x(t) \rangle$, which should represent the mean value of the hole ensemble in each band (implicitly assuming a rigid, localized k-space wave packet), using the same band structure and scattering models as for the MC simulations.

As the precise dynamics of ionization during the pump pulse is still an open issue to avoid introducing additional complications, we assume a fixed concentration $N_0 = 10^{14}$ cm^{-3} of band carriers during the pump pulse. Whereas this precludes an estimate of the absolute THG/FHG yields, it should still reveal important aspects of the HG process, whereas we can assess the accuracy of the description by
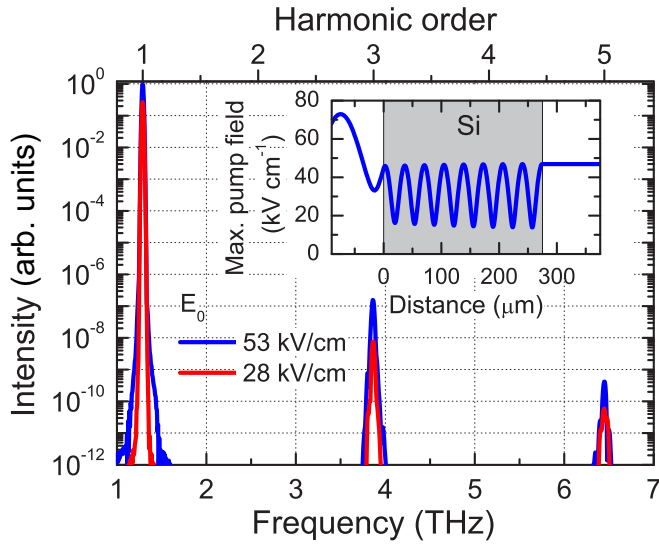
FIG. 3. MC-FDTD simulation: Intensity spectrum of the transmitted field corresponding to the highest experimental pump energy in Fig. 1 (blue curve, corresponding to an incident field $E_0 = 53$ kV/cm). Also included is the spectrum assuming a somewhat lower pump field of $E_0 = 28$ kV/cm to assess the pump-field dependence. The inset shows the peak pump-pulse field amplitude vs position z obtained from FDTD propagation, which shows the standing-wave effect due to internal reflections.

FIG. 4. Simulated intensity spectra of velocity $V(\nu)$ and wave-vector $K(\nu)$ for each band (top row: hh, bottom row: lh), using MC (left column) and simplified 1D$\langle k \rangle$ simulations (right column) for a nominal peak pump field of 24 kV/cm. Spectra normalized to respective peaks at the fundamental frequency. Ratios of peaks going from $K \rightarrow V$ for THG/FHG are included.

inspecting the THG:FHG intensity ratio, which should be less strongly affected by the time-dependent band population. Whereas the THz beam is quite tightly focused (see above), the Rayleigh range is sufficiently long relative to the sample thickness that we employ a plane-wave model (essentially treating the on-axis response). Even with the pump-induced ionization, the carrier density should be sufficiently low that one can neglect Drude reabsorption of radiation during propagation.

In order to assess the degree of quantitative agreement with the experiments above, we first present MC results including propagation effects for the pump beam, specifically to account for standing-wave effects in the sample due to internal reflections of the relatively long pump pulse (see below). For this treatment, we model the propagation of the pump pulse alone using linear finite-difference time-domain (FDTD) [20] to establish the time-dependent pump field vs position z, and then use this as the input to a set of parallel MC calculations for each z to yield the local band-weighted time-dependent velocity response $v(z, t)$ averaged over the ensemble. The total output field $E(t)$ is then calculated by summing over z with the appropriate relative phase delay. This approach is justifiable due to the weak depletion of the pump pulse and low carrier density (and, hence, weak pump-induced Drude effects) in the simulations. In Fig. 3, we show the resultant intensity spectrum of the emitted field exiting the sample, using an incident pump-pulse peak field of 53 kV/cm (outside the sample, corresponding to the highest estimated field of 24 kV/cm directly inside the sample in the experimental results above). Both THG and FHG peaks are clearly observed with a peak intensity ratio of 377:1, which is reasonably close to the ratio of 72:1 observed experimentally [Fig. 1(b)], considering the
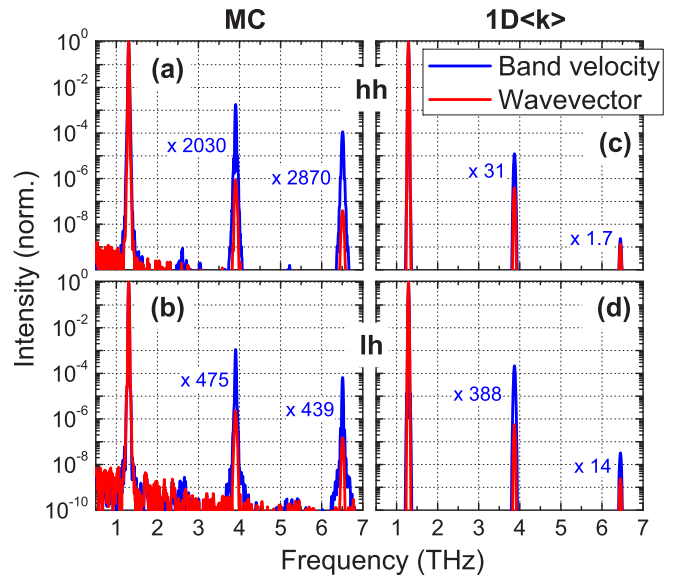
sensitive nonlinear dependence on the assumed parameters. Additional simulations assuming a lower pump peak field of 28 kV/cm (also included Fig. 3) yielded a ratio of 128:1. As shown in the inset, the standing-wave effects of the pump pulse in the sample are significant, which motivated the FDTD approach used here. As shown below, the 3HG:5HG intensities when considering only a single local z point are much closer (approaching 10:1). Hence, these quantitative results can only be obtained by accounting for the pump propagation effects and how this affects the relative phases of the 3HG and 5HG fields emitted at different positions in the sample.

We now turn to inspecting more closely the physical mechanisms contributing to the HG process by employing single-point simulations. As mentioned above, in addition to the MC simulations, we also carried out simulations for a rigid 1D wave packet to provide a reference to evaluate the roles of the three-dimensional (3D) carrier distribution and interband (i.e., lh-hh) scattering which are only incorporated in the MC model. In this 1D$\langle k \rangle$ model, we treat each band separately and numerically integrate the equation of motion for $\langle k \rangle(t)$ in the pump field $E(t)$ (both being the components along the Γ-X direction) via $\partial_t \langle k \rangle = (q/\hbar)E - \Gamma(\mathcal{E})\langle k \rangle$, where $\Gamma(\mathcal{E})$ is the instantaneous energy-dependent momentum scattering rate. The real-space velocity $v(t)$ for each band is then obtained via $v(t) = \hbar^{-1}\partial_k \mathcal{E}(t)$, which is taken as proportional to the (plane-wave) field emission [21]. To reduce artifacts in the scattering rate due to considering the scalar value for $\langle k \rangle$, $\Gamma(\mathcal{E})$ was convolved with a Gaussian function with a standard deviation of $2k_B T$.

The resultant intensity spectra for both methods and hh-/lh-bands are shown in Fig. 4, obtained from both the time-dependent velocity v and wave-vector $\langle k \rangle$, i.e., $V(\nu) = |\mathcal{F}\{v(t)\}|^2$ and $K(\nu) = |\mathcal{F}\{\langle k(t) \rangle\}|^2$, respectively. To better

inspect the relative peak intensities, we normalize all spectra to their respective peak value at the fundamental (pump) frequency. This allows one to assess *post facto* the relative roles of band anharmonicity vs energy-dependent scattering as $K(\nu)$ does not depend strongly on the band anharmonicity (i.e., only through its minor influence on the scattering rates compared to isotropic parabolic bands). As can be seen, the MC results predict drastically higher relative values for $V(\nu)$ for both THG/FHG and both bands, demonstrating the important role of band anharmonicity. A comparison of the MC results with the 1D$\langle k \rangle$ results shows significant deviations: in the latter: (i) the relative THG/FHG intensities are significantly lower, (ii) the role of anharmonicity is significant but much less so than in the MC results, and (iii) the lh-band THG/FHG intensities are significantly stronger than for the hh band.

We can account for these differences between the MC and 1D$\langle k \rangle$ results in the following analysis of the MC carrier distribution and 3D band structure. In Fig. 5 we plot the time dependence of the velocity in each band (weighted by their occupation fraction to represent their respective contribution to the total emitted field) after Fourier filtering of each harmonic component as well as the average wave-vector $\langle k_x \rangle$ (which follows the pump-pulse profile closely) and its rms spread both parallel (σ_x) and transverse ($\sigma_y = \sigma_z$) to the field polarization. We first note that the amplitude of the average k-space motion reaches values close to 0.04 (in units of $2\pi/a$), which correspond to energies of ~25 meV (hh) and ~40 meV (lh) (and corresponding temperatures of 195 and 300 K, respectively). This accounts for the dominant role of anharmonicity for our field regime as one does not yet reach the onset energy for scattering by phonon emission (64 meV for both LO/TO optical phonons at the Γ point). This also accounts for the lack of decay in $\langle k_x \rangle$ and σ_j in the trailing edge of the pump pulse: As the phonon scattering is dominated by low-energy acoustic phonons, the electron cooling is predicted to be on a timescale of more than 100 ps. Also, one observes that during the pump pulse, the spread of the carrier distribution grows from the initial level (dictated essentially by band filling at $T = 10$ K) to a higher nonequilibrium level in both the parallel and the transverse directions. An inspection of the velocity harmonics shows that the harmonic generation is stronger during the rising edge of the pulse with a complex pulse reshaping effect. Moreover, whereas the occupation-weighted velocity response is dominated by the hh contribution, one sees that the lh contribution is not negligible (addressed further below).

In order to assess how the neglect of the finite transverse carrier distribution might affect the predictions of the 1D$\langle k \rangle$ results, we also inspect the band structure away from the Γ-X axis. This is shown as a two-dimensional (2D) cross section vs (k_x, k_y) in Figs. 6(a) and 6(b) for each band with a magnified range of a higher-resolution calculation in Figs. 6(c) and 6(d). To examine the anharmonicity for driven motion parallel to k_x away from $k_y = 0$, we fit and subtract parabolas $p_y(k_x)$ for each k_y, and plot the anharmonic residuals in Figs. 6(e) and 6(f), with line-out curves in Figs. 6(g) and 6(h) for selected k_y values. These residuals show that the lh band has a stronger anharmonicity for $k_y = 0$, explaining why the 1D$\langle k \rangle$ results gave a dominant lh contribution in Figs. 4(c) and 4(d), whereas the anharmonicity grows rapidly for $k_y \neq 0$ with the
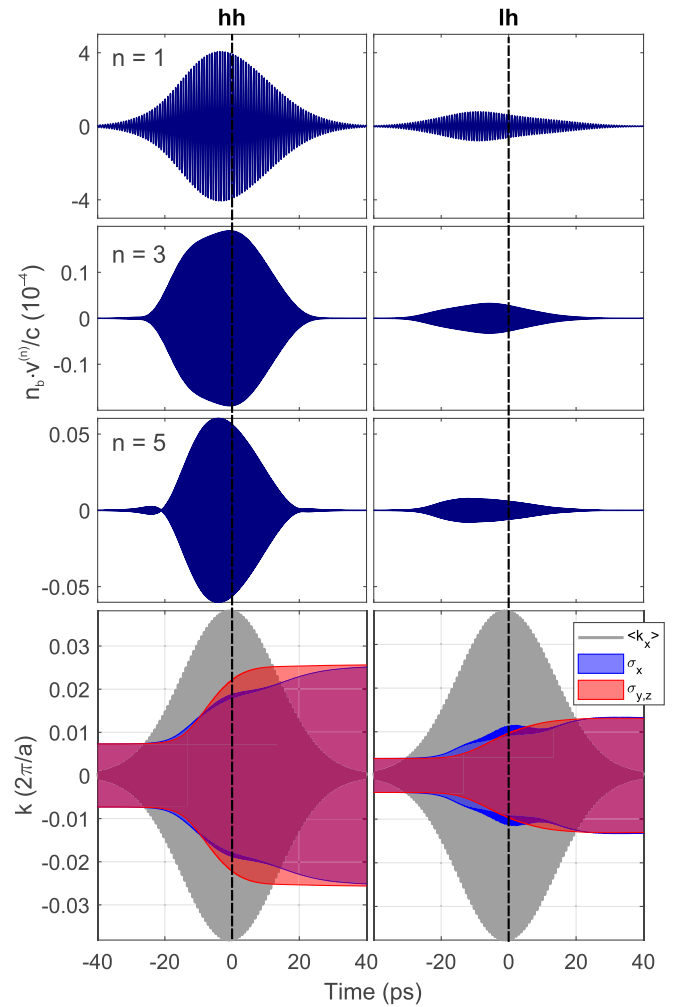

FIG. 5. Time-domain evolution of velocity components and carrier distribution. Top three rows: Filtered harmonic components (fundamental, THG, FHG; $n = 1, 3, 5$) of the occupation-weighted velocities for hh (left) and lh (right). Bottom row: Time dependence of the average wave-vector $\langle k_x \rangle$ (along the field direction, gray curve) and rms spread σ_j both parallel (σ_x) and transverse ($\sigma_{y,z}$) to the field direction ($\sigma_j^2 = \langle k_j^2 \rangle - \langle k_j \rangle^2$).

magnitude for the hh band becoming comparable to that of the lh band. Indeed, performing the 1D$\langle k \rangle$ simulations using the 1D band structure for $k_y \neq 0$ leads to a much stronger THG/FHG emission with levels similar to the MC results and the weighted hh contribution now dominating over the lh contribution (although additional artifacts emerge in the data, presumably due to the lack of distributional averaging in the scalar 1D simulations). In any case, this demonstrates that one must account for the extent of the time-dependent carrier distribution away from the field-polarization axis in order to correctly describe the dominant anharmonic response in the regime of our experiments.

We finally highlight some additional effects which are revealed by analyzing the MC results. In Figs. 7(a) and 7(b), we plot the harmonic velocity components $v^{(3,5)}(t)$ vs the fundamental one $v^{(1)}(t)$ (for a couple of cycles about the pump-pulse maximum) in order to inspect their phase relationship. These phases can be gauged by inspecting the
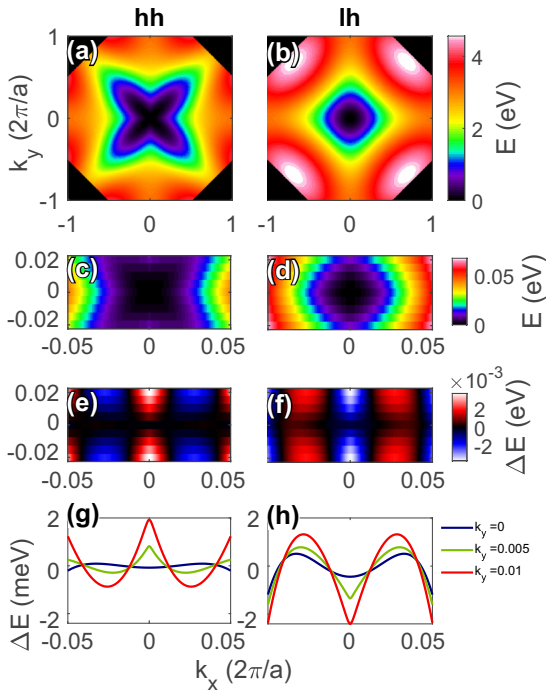
FIG. 6. (a) and (b) A 2D cross section of the full Brillouin zone for hh and lh, respectively, vs (k_x, k_y), demonstrating the well-known warped structure for each band. (c) and (d) Zoom into the k-space region relevant for the pump pulse fields considered here. (e) and (f) Residual after subtraction of parabolic fits $p_y(k_x)$ for each value of k_y, and (g) and (h) line outs of these residuals for selected k_y.

relative signs of $v^{(3)}$ and $v^{(1)}$ at the extreme points. (Note that the notion of a phase shift between waves of different frequency is only well defined with respect to chosen intracycle points of the fundamental wave, and we choose here the extrema of $v^{(1)}$.) One sees that for THG, whereas $v^{(3)}$ for the hh is essentially in phase with $v^{(1)}$ (corresponding to an "overshoot"), for the lh the fields are in antiphase (i.e., "clipping"). Indeed, when calculating the total weighted velocity (coherently summing the results in Fig. 5) the result is somewhat lower than for the hh alone. This phase relation is actually reversed for the FHG components, although the hh and lh contributions still remain in antiphase to each other. The key reason for this can indeed be traced back to the anharmonic band structure as shown in Figs. 6(e) and 6(h). One can see that for $k_y \neq 0$, the anharmonic residuals for hh and lh are of opposite signs, so one can expect that the harmonic responses of the two bands are indeed in antiphase. Lastly, we note that the band occupations change significantly during the pulse as shown in Fig. 7(c). This effect is also seen in DC MC simulations (not shown), and corresponds to a net lh → hh scattering for the nonequilibrium carrier distribution. This is expected due to the lower lh mass such that the lh inherently acquire more ponderomotive energy from the field (and, hence, have a higher temperature), leading to a net transfer of population to hh as the hh/lh attempt to establish thermal equilibrium. As shown in the inset, this interband transfer occurs at each peak of $k(t)$, i.e., twice per period of the pump field. To inspect the development of this effect during the pump pulse, we also plot the cycle-averaged relative interband scattering rate
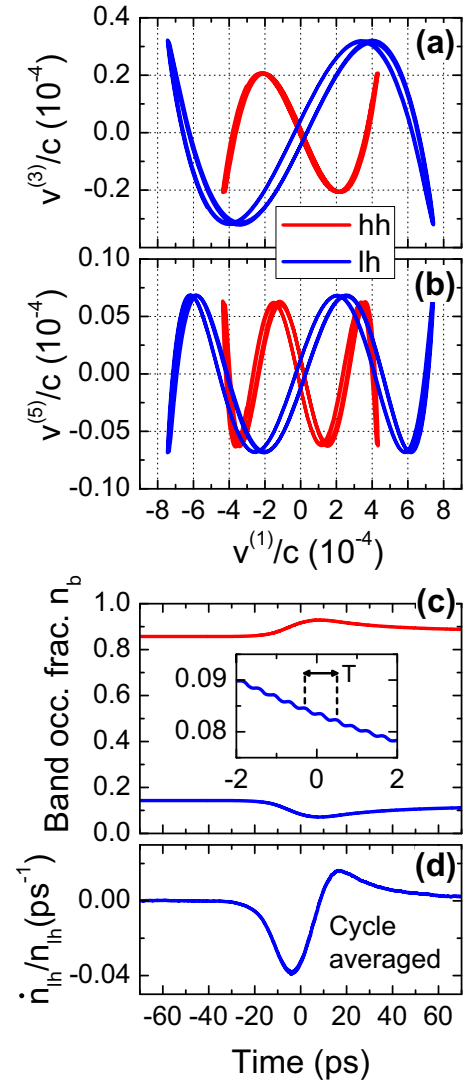

FIG. 7. MC simulations: Loci of the harmonic velocity components for (a) THG and (b) FHG plotted vs the fundamental component, for selected cycles about the pump-pulse maximum for both hh (red curves) and lh (blue). (c) Time-dependent population of hh and lh bands (the inset shows a zoomed range for the lh to better resolve the net intracycle lh → hh scattering that occurs about each peak in the magnitude of $\langle k \rangle (t)$, i.e., twice per fundamental period T). (d) Relative rate of change in lh population (cycle averaged).

for the lh, i.e., $n_{lh}^{-1} dn_{lh}/dt$, in Fig. 7(d). One sees that this normalized rate does not follow the shape of the pump pulse but rather saturates and reverts in sign near the peak of the pump pulse, which we attribute to the fact that both lh and hh have developed significant spread in the $k_{y,z}$ directions (see $\sigma_{y,z}$ in Fig. 5), which represent partial equilibration for those components of the kinetic energy not driven by the pump field. As this coherent interband scattering would also lead to an antiphase relation between hh and lh harmonics, we carried out additional MC simulations for isolated bands where this scattering mechanism cannot occur. However, the results were not changed significantly, and we can conclude that this effect does not play a significant role compared to the anharmonicity effects discussed above.

V. CONCLUSION

In conclusion, we have experimentally demonstrated third- and fifth-harmonic generation from Si:B, held at 10 K, upon excitation with intense FEL pulses at 1.29 THz and peak field strengths up to 24 kV/cm. Two main results are obtained. (i) The nonlinear susceptibilities show a strong dependence on the intensity of the terahertz pulses, which is indicative for an increase in the density of holes whereas a pulse is present. Model calculations support that the hole multiplication occurs by impact ionization of boron dopant atoms, initiated by thermally activated holes which are accelerated in the terahertz radiation field.

(ii) In addition, we have simulated the hole dynamics in the radiation field using time-domain MC simulations, which can reproduce aspects of the experimental emission quite well when including pump propagation effects and demonstrate that band anharmonicity dominates the HG process in our experimental regime, in particular, due to the strong nonparabolicity for carriers away from the field polarization axis.

This paper shows that high-field THz harmonic generation is highly sensitive to the precise anharmonicity of the band structure, and whereas it does not yield a direct characterization of the band structure, it does offer a complementary approach to other experimental and theoretical methods to treat the band-structure and energy-dependent momentum relaxation rates.

We declare that there are no conflicts of interest related to this article.

Data underlying the results presented in this paper are not publicly available at this time but may be obtained from the authors upon reasonable request.

[1] F. Meng, M. D. Thomson, Q. ul-Islam, B. Klug, A. Pashkin, H. Schneider, and H. G. Roskos, Intracavity third-harmonic generation in Si:B pumped by intense terahertz pulses, Phys. Rev. B **102**, 075205 (2020).

[2] Y. R. Shen, *Principles of Nonlinear Optics* (Wiley-Interscience, Hoboken, NY, 2002).

[3] C. K. N. Patel, R. E. Slusher, and P. A. Fleury, Optical Nonlinearities due to Mobile Carriers in Semiconductors, Phys. Rev. Lett. **17**, 1011 (1966).

[4] P. A. Wolff and G. A. Pearson, Theory of Optical Mixing by Mobile Carriers in Semiconductors, Phys. Rev. Lett. **17**, 1015 (1966).

[5] P. Kaw, Optical Mixing by Mobile Carriers in Semiconductors, Phys. Rev. Lett. **21**, 539 (1968).

[6] J. J. Wynne and G. D. Boyd, Study of optical difference mixing in Ge and Si using a CO_2 gas laser, Appl. Phys. Lett. **12**, 191 (1968).

[7] K. C. Rustagi, Effect of carrier scattering on nonlinear optical susceptibility due to mobile carriers in InSb, InAs, and GaAs, Phys. Rev. B **2**, 4053 (1970).

[8] C. C. Wang and N. W. Ressler, Nonlinear optical effects of conduction electrons in semiconductors, Phys. Rev. **188**, 1291 (1969).

[9] A. Mayer and F. Keilmann, Far-infrared nonlinear optics. ii. $\chi^{(3)}$ contributions from the dynamics of free carriers in semiconductors, Phys. Rev. B **33**, 6962 (1986).

[10] R. Brazis, R. Raguotis, and M. R. Siegrist, Suitability of drift nonlinearity in Si, GaAs, and InP for high-power frequency converters with a 1 THz radiation output, J. Appl. Phys. **84**, 3474 (1998).

[11] M. Urban, C. Nieswand, M. R. Siegrist, and F. Keilmann, Intensity dependence of the third-harmonic-generation efficiency for high-power far-infrared radiation in n-silicon, J. Appl. Phys. **77**, 981 (1995).

[12] B. S. Krishnamurthy and V. V. Paranjape, Note on optical mixing by mobile carriers in semiconductors, Phys. Rev. **181**, 1153 (1969).

[13] S. Ghimire and D. A. Reis, High-harmonic generation from solids, Nat. Phys. **15**, 10 (2019).

[14] P. J. Morin and J. P. Maita, Electrical properties of silicon containing arsenic and boron, Phys. Rev. **96**, 28 (1954).

[15] A. Dargys and S. Žurauskas, Tunnel ionization of shallow acceptors and donors in GaAs, J. Phys.: Condens. Matter **7**, 2133 (1995).

[16] C. Jungemann, S. Keith, M. Bartels, and B. Meinerzhagen, Efficient full band monte carlo hot carrier simulation for silicon devices, IEICE Trans. Electron. **82**, 870 (1999).

[17] C. Jungemann and B. Meinerzhagen, *Hierarchical Device Simulation: The Monte-Carlo Perspective*, Computational Microelectronics (Springer, Wien/New York, 2003).

[18] E. Ungersboeck, S. Dhar, G. Karlowatz, V. Sverdlov, H. Kosina, and S. Selberherr, The effect of general strain on the band structure and electron mobility of silicon, IEEE Trans. Electron. Devices **54**, 2183 (2007).

[19] M. Lundstrom, *Fundamentals of Carrier Transport*, 2nd ed. (Cambridge University Press, Cambridge, UK, 2009), digital version.

[20] K. Yee, Numerical solution of initial boundary value problems involving maxwell's equations in isotropic media, IEEE Trans. Antennas Propagation **14**, 302 (1966).

[21] W. Kuehn, P. Gaal, K. Reimann, M. Woerner, T. Elsaesser, and R. Hey, Terahertz-induced interband tunneling of electrons in GaAs, Phys. Rev. B **82**, 075204 (2010).

[22] P. Michel, ELBE Center for high-power radiation sources, J. large-scale research facilities (JLSRF), **2**, A39 (2016).